# Dual-Band Electrochromism in Hydrous Tungsten Oxide

Jenelle Fortunato<sup>1</sup>, Benjamin Z. Zydlewski<sup>3</sup>, Ming Lei<sup>4</sup>, Noah P. Holzapfel<sup>1</sup>, Matthew Chagnot<sup>1</sup>, James B. Mitchell<sup>1</sup>, Hsin-Che Lu<sup>2</sup>, De-en Jiang<sup>4</sup>, Delia J. Milliron<sup>2,3\*</sup>, & Veronica Augustyn<sup>1\*</sup>

<sup>1</sup> Dept. of Materials Science & Engineering, North Carolina State University, Raleigh, NC 27695, USA

<sup>2</sup> McKetta Dept. of Chemical Engineering, The University of Texas at Austin, Austin, TX, 78712, USA

<sup>3</sup> Dept. of Chemistry, The University of Texas at Austin, Austin, TX, 78712, USA

<sup>4</sup> Dept. of Chemical and Biomolecular Engineering, Vanderbilt University, Nashville, TN, 37235, USA

\*corresponding author, email: milliron@che.utexas.edu; vaugust@ncsu.edu

**Keywords**: electrochromism, tungsten oxide, structural water, spectroelectrochemistry, plasmon absorption

# **ABSTRACT**

The independent modulation of visible and near-infrared light by a single material, termed dualband electrochromism, is highly desirable for smart windows to enhance the energy efficiency of buildings. Tungsten oxides are commercially important electrochromic materials, exhibiting reversible visible and near-infrared absorption when electrochemically reduced in an electrolyte containing small cations or protons. The presence of structural water in tungsten oxides has been associated with faster electrochromic switching speeds. Here, we find that WO<sub>3</sub>·H<sub>2</sub>O, a crystalline hydrate, exhibits dual-band electrochromism unlike the anhydrous WO<sub>3</sub> providing a heretofore unexplored route to tune the electrochromic response of tungsten oxides. Absorption of nearinfrared light is achieved at low Li<sup>+</sup>/e<sup>-</sup> injection, followed by the absorption of visible light at higher Li<sup>+</sup>/e<sup>-</sup> injection as a result of an electrochemically-induced phase transition. We propose that this dual-band modulation is possible due to the more open structure of WO<sub>3</sub>·H<sub>2</sub>O as compared to WO<sub>3</sub>. This facilitates a more extended solid solution Li<sup>+</sup> insertion regime that benefits the modulation of near-infrared radiation via plasmon absorption. Higher degrees of Li<sup>+</sup>/e<sup>-</sup> insertion lead to polaronic absorption associated with localized charge storage. These results inform how structural factors influence the electrochemically induced spectral response of transition metal oxides and the important role of structural water beyond optical switching speed.

# INTRODUCTION

Electrochromic materials, commonly transition metal oxides (TMOs), modulate their optical properties in response to an applied electrical potential in the presence of an electrolyte. The ability to reversibly tune properties such as optical transmission, absorbance, or reflectance makes TMOs an important class of materials for dynamic window glazings and could lead to significant energy savings. Dynamic windows (e.g., "smart windows") can provide building occupants with greater control over heating, cooling, daylighting, and privacy by modulating the influx of solar radiation. Of particular interest is the development of single materials that can control the transmittance of visible and near-infrared (NIR) light independently, allowing for selective, dual-band control over lighting and heating from solar radiation.<sup>2</sup> Electrochromic materials can achieve a dual-band response via two distinct electrochemical processes that give rise to either a polaronic (visible) or surface plasmonic (NIR) response.<sup>3</sup> The polaronic response arises from localized charge storage compensated by the insertion of an ion into the bulk of the material. It is coupled to a distortion of the solid TMO host, which can include first-order phase transformations. The polaronic mechanism triggers changes in the visible light absorbance due to the formation of an electronic polaron band below the conduction band minimum. The plasmonic response is associated with delocalized charging of the TMO that can give rise to absorption or reflection due to surface plasmon resonance. Surface plasmons modulate optical absorption via collective oscillation at the localized surface plasmon resonance (LSPR) frequency, manifesting as light extinction in the NIR region owing to the moderate charge densities in the TMO.<sup>3</sup> Surface plasmonic charge can be compensated via ion adsorption in the electric double layer and doesn't induce significant structural distortions in the material. The structure of TMOs plays an integral role in determining the nature of the electrochromic response.<sup>4–9</sup>

The tungsten oxides are a well-known family of electrochromic TMOs that exhibit blue coloration upon electrochemical reduction and reversible bleaching upon oxidation in electrolytes containing small cations (e.g., Li<sup>+</sup>, Na<sup>+</sup>) or protons.<sup>10</sup> The use of tungsten oxides and other TMOs for dual-band electrochromism has been shown previously (**Table S1**), but understanding factors that influence the electrochromic response, including dual-band electrochromism, is important for the application of tungsten oxides in electrochromic devices. For example, Heo et al. showed that selectively inserting cations into optically active hexagonal interstitial sites increases the coloration efficiency of monoclinic WO<sub>2.72</sub>, compared to cation insertion into square or trigonal interstitial sites.<sup>6</sup>

Another factor considered for modulating the electrochromic response of tungsten oxides is the presence of structural water. Structural water exists in a number of tungsten oxide polymorphs synthesized in aqueous conditions, such as hexagonal WO<sub>3</sub> (h-WO<sub>3</sub>) and tungsten oxide hydrates (WO<sub>3</sub>·H<sub>2</sub>O and WO<sub>3</sub>·2H<sub>2</sub>O). The positive role of structural water on the kinetics of proton and cation insertion into tungsten oxides has been reported for decades.<sup>5,11,12</sup> For electrochromic applications, faster ion insertion is useful to obtain faster switching speeds. The kinetic improvement has been ascribed to fast ion transport along structural water networks. For example, Wang et al. proposed that WO<sub>3</sub>·2H<sub>2</sub>O showed better kinetics and NIR electrochromic properties than WO<sub>3</sub> due to its "high speed pathways for cation insertion."<sup>13</sup> However, we reported that the structural stability of tungsten oxide hydrates during ion insertion is an alternate explanation for their fast kinetics since less structural deformation is inherently coupled to faster electrochemical kinetics.<sup>14,15</sup> Less well understood than the kinetic effect associated with solid state ion transport is the role that structural water in tungsten oxide may play on the electrochromic coloration mechanisms and the dual-band response, a result not previously reported. The

presence of structural water in the solid state can affect the TMO electronic structure. For example, Shi et al. found that structural water contributes to the band structure of WO<sub>3</sub>·2H<sub>2</sub>O and acts as a weak electron donor by participating in ligand-to-metal charge transfer, thereby enhancing photon absorption.<sup>16</sup>

Here, we compared the electrochromic response of orthorhombic WO<sub>3</sub>·H<sub>2</sub>O with monoclinic WO<sub>3</sub> understand the influence of structural water beyond kinetics. spectroelectrochemistry along with a suite of physical and electrochemical techniques, together with density functional theory (DFT) simulations, to understand the mechanisms involved. We show that unlike WO<sub>3</sub>, WO<sub>3</sub>·H<sub>2</sub>O exhibits a dual-band electrochromic response. We propose that the presence of structural water facilitates capacitive-like behavior at low charge injection, inducing optical modulation in the NIR region. Absorbance in the visible region is initiated by an electrochemically-induced phase-transition in WO<sub>3</sub>·H<sub>2</sub>O at high charge injection, which leads to localized charge storage and polaron absorption. We show that structural water in tungsten oxides is an effective strategy for designing electrochromic TMO materials that exhibit a dual-mode electrochromic response for independent modulation of visible and NIR light. Such materials could lead to more energy efficient buildings in the future.

# **EXPERIMENTAL SECTION**

# Thin film deposition

WO<sub>3</sub>·H<sub>2</sub>O and WO<sub>3</sub> thin films were synthesized in a two-step process consisting of the electrodeposition of a WO<sub>3</sub>·2H<sub>2</sub>O thin film followed by its thermal dehydration, as described previously. <sup>15,17</sup> Electrodeposition was performed in a 3-electrode cell with a potentiostat (BioLogic,

MPG2). The electrochemical cell consisted of a 50 mL glass three-neck round-bottom flask with a Ag/AgCl reference electrode (4 M KCl, Pine Research) and a Pt wire (99.99% purity, Alfa Aesar) counter electrode. A WO<sub>3</sub>·2H<sub>2</sub>O film was electrodeposited onto a 1 cm² area of cleaned fluorinated tin oxide (FTO, Sigma Aldrich) coated glass that served as the working electrode following a previously reported procedure. <sup>18</sup> The electrodeposition solution consisted of 12 mM Na<sub>2</sub>WO<sub>4</sub>·2H<sub>2</sub>O and 0.5 M H<sub>2</sub>SO<sub>4</sub>. It was prepared immediately before the electrodeposition by heating ~25 mL of a 12 mM Na<sub>2</sub>WO<sub>4</sub>·2H<sub>2</sub>O (Sigma Aldrich) aqueous solution to 75°C. Once it reached 75°C, 680 μL of concentrated (18.4 M) H<sub>2</sub>SO<sub>4</sub> (Fisher Scientific) was added to obtain a concentration of 0.5 M H<sub>2</sub>SO<sub>4</sub>. The deposition solution was transferred to the three-neck flask and electrodeposition was performed via cyclic voltammetry using a potential window of -0.3 – 0.8 V vs Ag/AgCl at a scan rate of 100 mV s<sup>-1</sup> for 250 cycles (~3 hours). After electrodeposition, the WO<sub>3</sub>·2H<sub>2</sub>O film was rinsed with DI H<sub>2</sub>O and aged for 24 hours in 0.5 M H<sub>2</sub>SO<sub>4</sub>. The electrode was heated at 120°C in air for 72 hours to obtain the monohydrate WO<sub>3</sub>·H<sub>2</sub>O film. To obtain the anhydrous WO<sub>3</sub> film the electrode was heated at 300°C in air for 20 hours.

# Physical characterization

Phase identification was performed using XRD on a Rigaku SmartLab X-Ray Diffractometer in the grazing incidence operating mode equipped with a graphite monochromator which selects only Cu K $\alpha_1$  radiation ( $\lambda$ = 1.5406 Å). Pawley refinements of the diffraction data were carried out using the TOPAS-Academic (Version 6) software package to determine the lattice parameters.<sup>19</sup> Crystal structure images were generated with the VESTA 3 software.<sup>20</sup> SEM was performed using a field emission FEI Verios 460L microscope. Phase identification was also performed with Raman spectroscopy using a WITec alpha 300R confocal Raman spectrometer (WITec Instruments Corp, Ulm, Germany) equipped with a 532 nm Nd: Yag laser, and an 1800 groove

cm<sup>-1</sup> grating (spectral resolution ~1 cm<sup>-1</sup>). Laser excitation was focused through a 100x Zeiss objective lens. Laser wavelength was calibrated from the Raman spectrum of a single-wave Si wafer with a characteristic peak at 520 cm<sup>-1</sup>. Film thickness was measured with laser profilometry using a Keyence VKx1100 Confocal Laser Scanning Microscope (CLSM).

# **Spectroelectrochemistry**

Spectroelectrochemical data was collected in situ using a quartz cell inside of an Ar-filled glovebox coupled to a BioLogic VMP3 potentiostat and an ASD Quality Spec Pro UV-Vis-NIR spectrometer. The data was collected using electrolytes consisting of either 1.0 M lithium perchlorate (LiClO<sub>4</sub>, dry, 99.99% trace metals, Sigma Aldrich) in propylene carbonate (PC, anhydrous, 99.7%, Sigma Aldrich) or 0.1 M tetrabutylammonium perchlorate (TBACIO<sub>4</sub>, 99.0% purity, Sigma Aldrich) in propylene carbonate. All electrolytes were prepared and used inside an Ar-filled glovebox to prevent air and water contamination. For measurements in LiClO<sub>4</sub> electrolyte, a Li foil electrode was used as both the counter and reference electrodes. For measurements in TBACIO4 electrolyte, a Ag/Ag+ reference electrode and Pt foil counter electrode were used. The initial electrochromic response of WO<sub>3</sub> and WO<sub>3</sub>·H<sub>2</sub>O thin films were characterized using chronoamperometry. The transmittance was monitored as a function of the applied potential to determine the potential window which led to an electrochromic response. The coloration efficiency, which is the ratio of the change in optical density to the stored aerial charge density, was measured using chronopotentiometry. A constant current equivalent to ~1C rate was selected to allow for monitoring of small changes in transmittance as a function of injected charge. The slopes of the plots of the change in optical density vs. charge density were used to determine the coloration efficiency. All transmittance values were background subtracted to FTO-coated glass immersed in the appropriate electrolyte.

# **Electrochemical Characterization**

Electrochemical characterization was performed with a 3-electrode cell and a potentiostat (BioLogic, VMP3) in an argon-filled glovebox with H<sub>2</sub>O and O<sub>2</sub> levels < 1 ppm. Electrochemical experiments were performed in 1 M LiClO<sub>4</sub> (dry, 99.99% trace metals, Sigma Aldrich) in propylene carbonate (PC, anhydrous, 99.7%, Sigma Aldrich) and 0.1 M TBAClO<sub>4</sub> (99.0% purity, Sigma Aldrich) in PC. A concentration of 0.1 M was chosen for TBAClO<sub>4</sub> in PC due to the solubility limit of TBAClO<sub>4</sub> in non-aqueous electrolytes. The electrochemical cell consisted of a 50 mL glass three-neck round bottom flask with a Li metal (99.99% trace metals, Sigma Aldrich) counter electrode for experiments in LiClO<sub>4</sub> and a Pt wire counter electrode for experiments performed in TBAClO<sub>4</sub>. Cyclic voltammetry was used to determine areal capacity and coulombic efficiency, and to correlate electrochemical signatures to the spectral response. Areal capacity was normalized to the geometric area of the deposited electrode (A = 1 cm<sup>2</sup>).

# **Computational modeling**

Spin-polarized DFT calculations were performed by using the Vienna ab initio simulation package (VASP 5.4.4).<sup>21</sup> Projector augmented wave (PAW) potentials were used to treat the electron-ion interaction, with a cutoff of 500 eV for the plane waves. The Perdew-Burke-Ernzerhof (PBE) functional within the generalized gradient approximation (GGA) for electron exchange-correlation was used for geometry optimization.<sup>22</sup> Grimme's DFT + D3 method was used to account for the van der Waals interactions. The convergence criteria for energy and force were set as  $10 \times ^{-5}$  eV and  $0.01 \text{ eV} \cdot \text{Å}^{-1}$ , respectively. The Brillouin zone was sampled with a  $5 \times 5 \times 5$  Monkhorst-Pack grid for both WO<sub>3</sub> and WO<sub>3</sub>·H<sub>2</sub>O structures. As informed from the experimental characterization of the structures (**Figure S1** and **Table S2**) and compositions, the DFT-optimized lattice parameters before and after Li-ion insertion are shown in **Table S3**.

The hybrid functional of Heyd-Scuseria-Ernzerhof (HSE06) was used for the optical property calculation.<sup>23</sup> The relationship between the absorption coefficient  $\alpha$ , spectral transmittance  $T(\lambda)$  and reflectance  $R(\lambda)$  is described as follows:<sup>24</sup>

$$\alpha(\lambda) = \frac{1}{d} \ln \left( \frac{1 - R(\lambda)}{T(\lambda)} \right) \ln \left( \frac{1 - R(\lambda)}{T(\lambda)} \right), \tag{1}$$

where  $\lambda$  is the wavelength and d represents the thickness of the film (obtained from the experiments). We extracted the absorption coefficient  $\alpha$  and reflectance  $R(\lambda)$  from the DFT-computed frequency-dependent dielectric function using VASPKIT.<sup>25</sup>

# **RESULTS AND DISCUSSION**

# Physical characterization of WO<sub>3</sub>·H<sub>2</sub>O and WO<sub>3</sub> films

We synthesized thin film electrodes of  $WO_3 \cdot H_2O$  and  $WO_3$  and compared their electrochromic response to understand the influence of structural water on the optoelectronic properties of tungsten oxides. Orthorhombic  $WO_3 \cdot H_2O$  has a 2D network of  $WO_5(OH_2)$  octahedra with terminal water molecules occupying the interlayer space, whereas monoclinic  $WO_3$  has a distorted  $ReO_3$  structure composed of corner sharing  $WO_6$  octahedra (**Figure 1**).<sup>26,27</sup>

To synthesize the electrode films, we first electrodeposited monoclinic WO<sub>3</sub>·2H<sub>2</sub>O onto FTO-coated glass and then thermally dehydrated this material to obtain orthorhombic WO<sub>3</sub>·H<sub>2</sub>O and monoclinic WO<sub>3</sub> films. We did not characterize the electrochromic response of WO<sub>3</sub>·2H<sub>2</sub>O because it transforms to WO<sub>3</sub>·H<sub>2</sub>O upon exposure to the non-aqueous electrolytes used here.<sup>28</sup> Grazing incidence X-ray diffraction (GIXRD) and Raman spectroscopy were used to determine the structure of each film. Phase analysis of the GIXRD patterns for WO<sub>3</sub>·H<sub>2</sub>O and WO<sub>3</sub> films match well with the reported structures for WO<sub>3</sub>·H<sub>2</sub>O (PDF 00-043-0679) and WO<sub>3</sub> (PDF 01-083-0950), respectively. Pawley refinements of the GIXRD data show some variation in lattice parameters for both compositions, with WO<sub>3</sub>·H<sub>2</sub>O having a greater degree of deviation from the

indexed structure **Figure S1**). This deviation could be due to strain effects from the FTO substrate. The peak around 16.3° 20 in the WO<sub>3</sub>·H<sub>2</sub>O pattern corresponds to the (020) lattice plane representing an interlayer distance of ~0.54 nm, in agreement with previous work.<sup>29</sup> Raman spectroscopy shows the characteristic peaks for WO<sub>3</sub>·H<sub>2</sub>O (**Figure S2**) with a broad peak between 550 and 750 cm<sup>-1</sup> corresponding to the in-plane O–W–O stretching ( $\nu$ ) modes and a sharp peak around 945-950 cm<sup>-1</sup> corresponding to the tungsten-to-terminal oxygen  $\nu$ (W–O<sub>t</sub>) mode.<sup>29,30</sup> For WO<sub>3</sub>, Raman spectroscopy shows the expected peaks for the O–W–O bending mode ( $\delta$ ) around 275 cm<sup>-1</sup> and  $\nu$ (O–W–O) around 700 and 800 cm<sup>-1</sup> (**Figure S2**).<sup>30</sup>

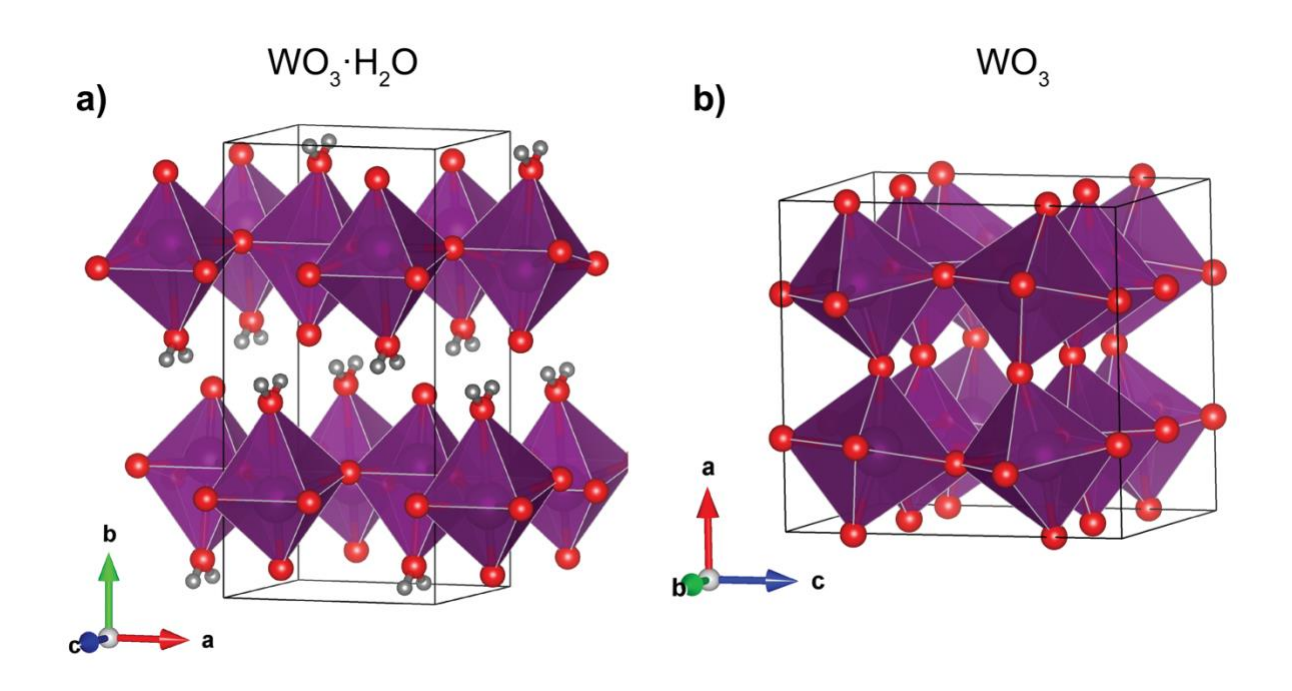


**Figure 1.** Schematic representation of the crystal structures for (a)  $WO_3 \cdot H_2O$  and (b)  $WO_3$ . Structural water leads to a 2D layered structure in  $WO_3 \cdot H_2O$  with an interlayer distance of ~0.54 nm.

SEM images show that both electrodes consist of a homogeneous film of particles across the electrodeposition area (**Figure 2**). The particles exhibit a platelet-like morphology due to the layered structure of the parent material, WO<sub>3</sub>·2H<sub>2</sub>O. Its preservation at higher temperatures

indicates that thermal dehydration of  $WO_3 \cdot 2H_2O$  to  $WO_3 \cdot H_2O$  and  $WO_3$  proceeds via topotactic reactions. The platelet size is slightly smaller for  $WO_3 \cdot H_2O$  than  $WO_3$  probably as a result of grain growth at the higher dehydration temperature for  $WO_3$ . Laser profilometry was used to measure the thickness of the deposited films. The film thickness of  $WO_3 \cdot H_2O$  was  $243 \pm 34$  nm and for  $WO_3$  it was  $78.5 \pm 0.7$  nm (**Figure S3**). The decrease in the film thickness occurs from crystal structure transformation as well as mesoscale densification. The unit cell density from GIXRD patterns is 5.70 g cm<sup>-3</sup> for  $WO_3 \cdot H_2O$  and 7.38 g cm<sup>-3</sup> for  $WO_3 \cdot$  the increase in density is expected upon the removal of structural water. The remaining difference in thickness is ascribed mesoscale densification, changing the overall pore volume fraction, though both films retain a highly porous morphology based on their appearance by SEM.

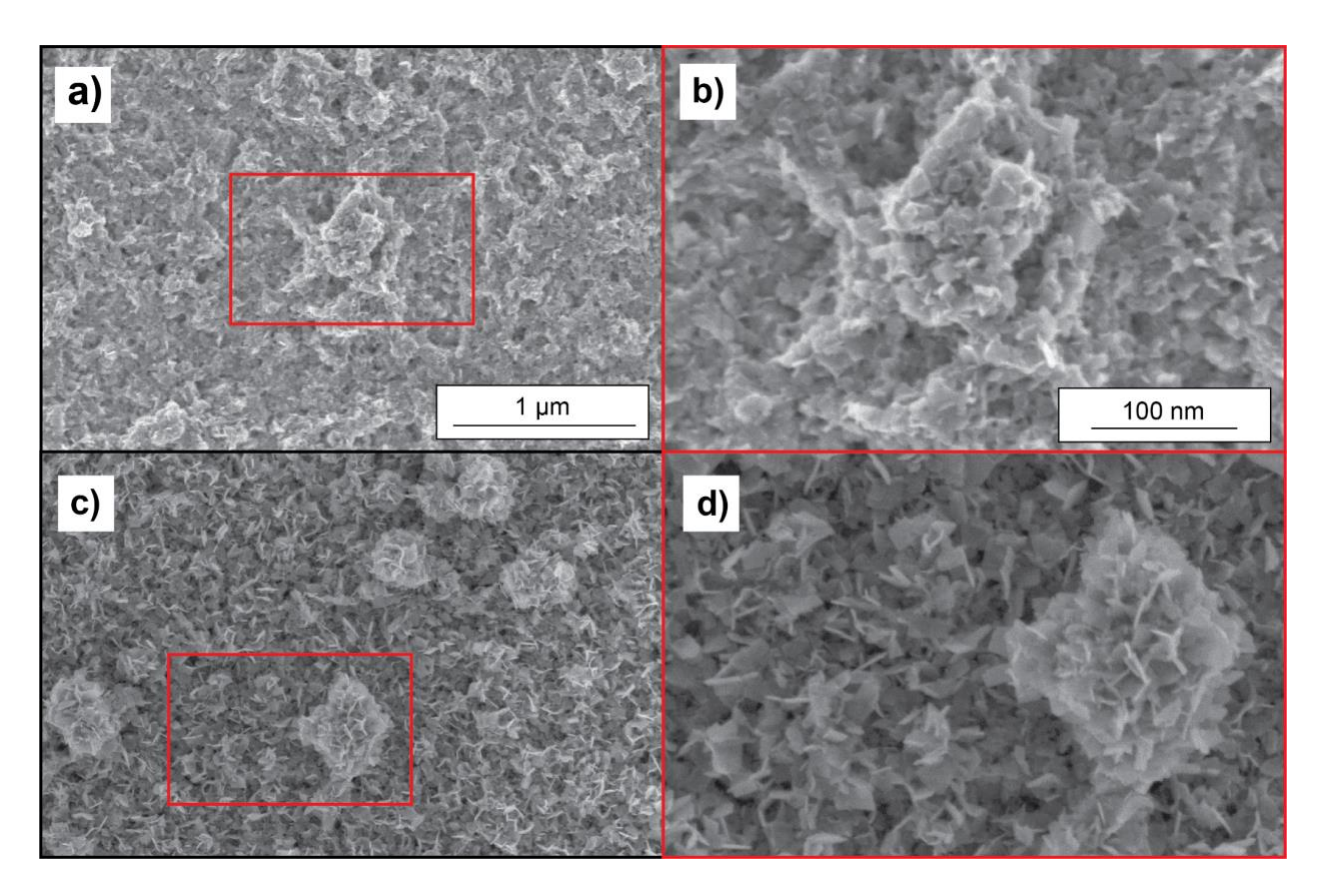


**Figure 2.** SEM of pristine  $WO_3 \cdot H_2O$  (a, b) and  $WO_3$  (c, d) thin films showing that both consist of nanoscale platelets. The smaller platelet size of  $WO_3 \cdot H_2O$  is due to its lower dehydration temperature (120°C) as compared to  $WO_3$  (300°C).

# Spectroelectrochemical characterization

Spectroelectrochemistry was used to determine the electrochromic response of  $WO_3 \cdot H_2O$  and  $WO_3$  films in 1 M LiClO<sub>4</sub> and 0.1 M TBAClO<sub>4</sub> in PC electrolytes. These electrolytes were selected to compare the influence of cation insertion on the electrochromic response. Due to its small ionic radius, Li<sup>+</sup> (radius = 76 pm) can participate in charge-compensation at the surface and within the bulk via insertion reactions, whereas TBA<sup>+</sup> (radius = 494 pm) can only participate at the surface.<sup>6,7</sup> Electrochemical charge compensation with  $WO_3 \cdot H_2O$  and  $WO_3$  can be expressed as:

$$WO_3 \cdot H_2O$$
;  $WO_3 + xM^+ + xe^- \leftrightarrow M_xWO_3 \cdot H_2O$ ;  $WO_3 \quad (0 \le x \le 1)$  (2)

where x is the number of electrons and M<sup>+</sup> is the electrolyte cation (here, M<sup>+</sup> = Li<sup>+</sup> or TBA<sup>+</sup>). <sup>14,31</sup> For reversible electrochromism of tungsten oxides, x is generally limited to a maximum of 1 (e.g. when all W<sup>6+</sup> is reduced to W<sup>5+</sup>). Chronoamperometry was used to poise the film electrodes at varying states of charge and optical spectra were collected from the visible (VIS) to the infrared (IR) (350 – 2000 nm) to assess the electrochromic response of each material. The thin films started in the oxidized state and were systematically reduced in 1 M LiClO<sub>4</sub> in PC from 4.0 V vs Li/Li<sup>+</sup> to 1.4 V and 1.6 V for WO<sub>3</sub>·H<sub>2</sub>O and WO<sub>3</sub>, respectively. Overall, the transmittance (T) declines for both upon reduction in the Li<sup>+</sup> electrolyte and transparency is recovered upon reoxidation (**Figure 3a and b**).

The kinetics of the coloration process were analyzed following a step change in the potential by coloring or bleaching the thin films to fully reduced or oxidized states to assess the overall rate of the coloration process. For both films in the Li<sup>+</sup> electrolyte, the coloration and bleaching processes were completed within 15 seconds, indicating rapid switching kinetics (**Figure S4**). Livage et al.

observed kinetic differences between hydrous and anhydrous WO $_3$  films to achieve a 50% change in absolute transmission in 1 M LiClO $_4$  in PC (10 s for WO $_3$ ·H $_2$ O, 35 s for WO $_3$ ). The lack of a kinetic difference in our case indicates that any kinetic differences may be present at faster times (< 15 seconds). Since a switching time of ~ 15 s is sufficient for electrochromic applications, we did not probe faster switching times here. In 0.1 M TBAClO $_4$ , the coloration process was slightly slower in both materials. The lower electrolyte concentration of TBAClO $_4$  vs. LiClO $_4$  could be the cause of the slower coloration process (**Figure S5**).

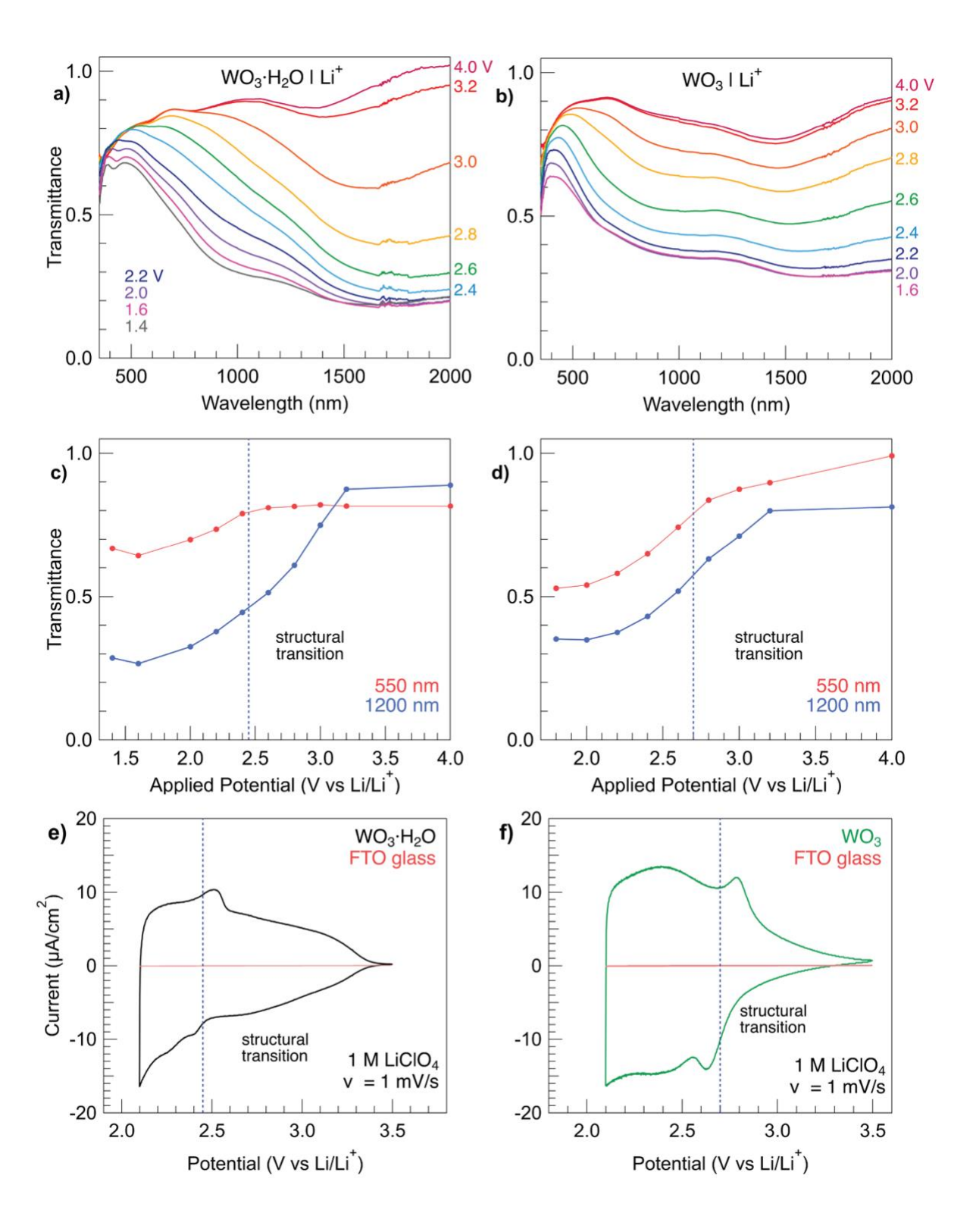


**Figure 3.** Spectroelectrochemistry of  $WO_3 \cdot H_2O$  (a, c, e) and  $WO_3$  (b, d, f) in 1 M LiClO<sub>4</sub> in PC as a function of applied potential. a, b) Optical transmittance across the VIS-NIR spectrum as a function of applied potential for  $WO_3 \cdot H_2O$  and  $WO_3$ , respectively. c, d) Linear plots of optical transmittance at 550 nm (red, visible region) and 1200 nm (blue, NIR region) as a function of applied potential. e, f) Cyclic voltammograms of  $WO_3 \cdot H_2O$  and  $WO_3$  at 1 mV s<sup>-1</sup> in 1 M LiClO<sub>4</sub> in PC.

We further compared the optical changes in the visible and NIR regions by monitoring changes in transmittance as a function of applied potential at 550 nm (visible) and 1200 nm (NIR) (Figure 3c, d; Table 1, Figure S6). For WO<sub>3</sub>·H<sub>2</sub>O at 550 nm, there is no change in the transmittance as the material is reduced from 4.0 to 2.6 V (T = 0.82). Once the material is reduced below 2.6 V the transmittance declines from T = 0.82 to 0.69 ( $\Delta T_{VIS}$  = -0.13, **Figure 3c**, red trace, **Figure S6a**). Conversely, at 1200 nm the transmittance declines early in the reduction process (3.2 V; T = 0.88) and continues to decline reaching T = 0.29 at 1.6 V ( $\Delta T_{NIR}$  = -0.59, **Figure 3c**, blue trace, **Figure S6a**). These results demonstrate that WO<sub>3</sub>·H<sub>2</sub>O shows a dual-band electrochromic response in the visible and NIR regions that is dependent on the amount of Li<sup>+</sup> injected into the material. Changes in the NIR begin at small amounts of charge injection (i.e., higher potentials), whereas changes in the visible begin at comparatively higher amounts of charge injected (i.e., lower potentials). We performed the same comparison for WO<sub>3</sub>, which showed a simultaneous decline in transmittance at 550 nm and 1200 nm during reduction from 4.0 to 1.6 V. The transmittance for visible (550 nm) and NIR (1200 nm) declined from T = 0.99 and 0.81 to T = 0.53 and 0.35, respectively ( $\Delta T_{VIS}$  = -0.46 and  $\Delta T_{NIR}$  = -0.46; **Table 1, Figure S6b**). These results demonstrate that WO<sub>3</sub> does not exhibit dual-band electrochromic behavior and instead has a broadband optical response to electrochemical reduction (Figure 3d).

**Table 1.** Change in transmittance ( $\Delta T = T_x - T_0$ ) for WO<sub>3</sub>·H<sub>2</sub>O and WO<sub>3</sub> in 1 M LiClO<sub>4</sub> and 0.1 M TBAClO<sub>4</sub> in PC.  $\Delta T_{VIS}$  was determined at 550 nm and  $\Delta T_{NIR}$  at 1200 nm.

Electrolyte	WO <sub>3</sub> ·H <sub>2</sub> O		WO <sub>3</sub>	
	ΔTvis	$\DeltaT_{NIR}$	ΔTvis	$\Delta T_{NIR}$
1 M LiClO <sub>4</sub> in PC	-0.13	-0.59	-0.46	-0.46
0.1 M TBACIO <sub>4</sub> in PC	0.00	-0.26	-0.02	-0.19

The same spectroelectrochemical analysis was performed for each material in 0.1 M TBACIO<sub>4</sub> in PC to assess the influence of cation insertion on optical changes (Figure 4a and b). In both films, no appreciable changes in transmittance were seen at 550 nm upon reduction from 1.0 to -1.4 V  $(\Delta T_{VIS, WO3 \cdot H2O} = 0.0 \text{ and } \Delta T_{VIS, WO3} = -0.02$ ; Figure 4c and d; Table 1). Conversely, at 1200 nm the transmittance declined in both materials over the entirety of the reduction window ( $\Delta T_{NIR}$ .  $w_{O3-H2O}$  = -0.26 and  $\Delta T_{NIR}$ ,  $w_{O3}$  = -0.19; Figure 4c and d; Table 1). Comparing the spectroelectrochemistry results in LiClO<sub>4</sub> and TBAClO<sub>4</sub> helps to identify the role of surface versus insertion processes for modulating optical changes. First, the lack of optical changes in the visible for WO<sub>3</sub>·H<sub>2</sub>O and WO<sub>3</sub> in TBA<sup>+</sup> indicates that cation insertion is necessary for modulating transmittance in the visible region, as expected for the polaronic process. Second, optical changes in the NIR for WO<sub>3</sub>·H<sub>2</sub>O and WO<sub>3</sub> are modulated by both surface and insertion reactions, which is evident by the small reduction in NIR transmittance in TBA+ and an over 2x greater decrease in transmittance in the Li<sup>+</sup> (in WO<sub>3</sub>·H<sub>2</sub>O, ΔT<sub>NIR</sub> = -0.26 for TBA<sup>+</sup> compared to -0.59 for Li<sup>+</sup>; in WO<sub>3</sub>,  $\Delta T_{NIR}$  = -0.19 for TBA<sup>+</sup> compared to -0.46 for Li<sup>+</sup>). The overall change in NIR transmittance is smaller in TBA+ compared to Li+: TBA+ is limited by the electrochemical surface area of the films, whereas Li<sup>+</sup> can utilize both the surface and bulk for modulating NIR transmittance. Collectively, these results show that both WO<sub>3</sub>·H<sub>2</sub>O and WO<sub>3</sub> utilize the bulk and surface for charge compensation with Li<sup>+</sup>, and that WO<sub>3</sub>·H<sub>2</sub>O exhibits a dual-band electrochromic response whereas WO<sub>3</sub> has a single-band response. These results indicate that the presence of structural water leads to the dual-band electrochromic response of WO<sub>3</sub>·H<sub>2</sub>O.

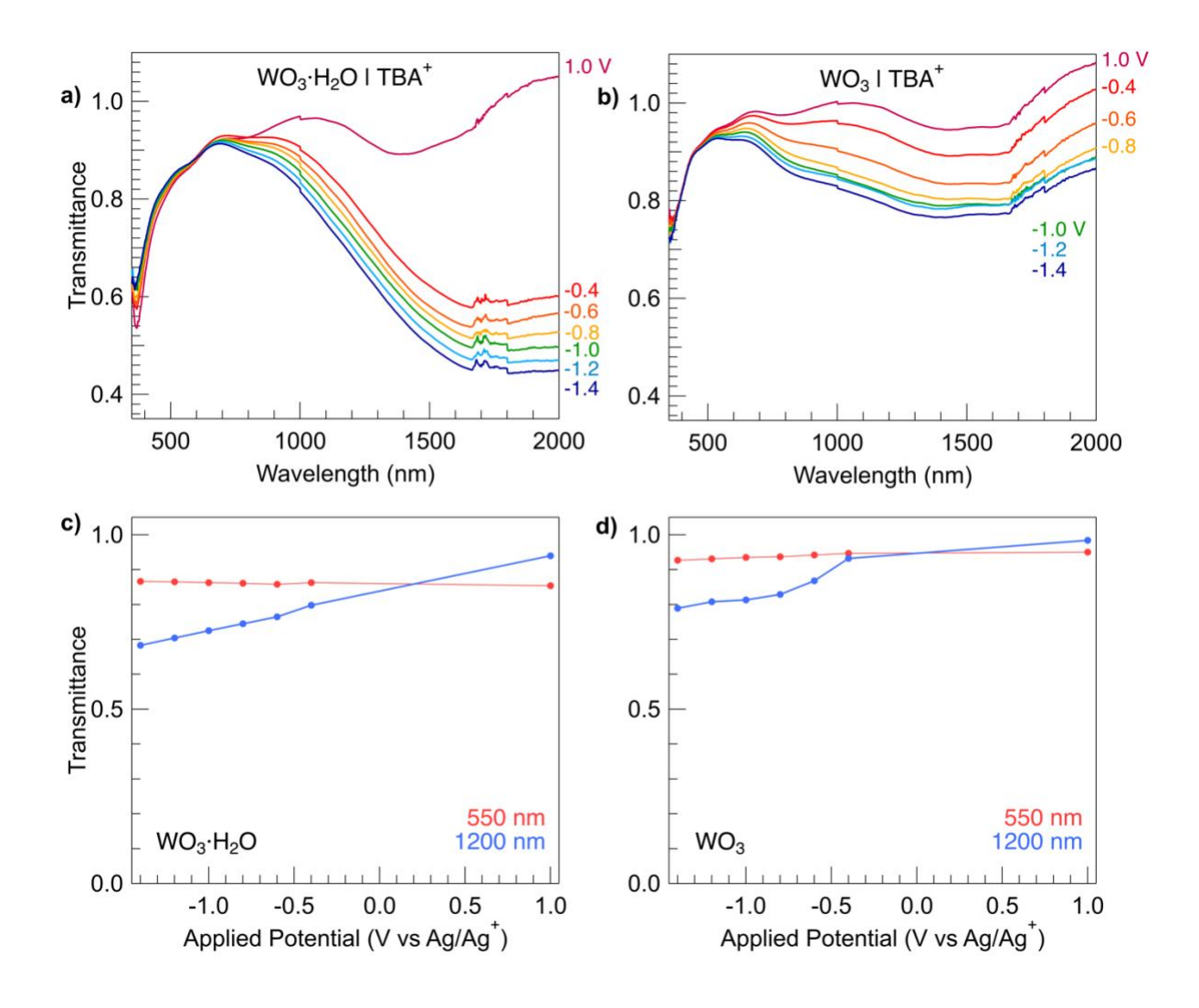


**Figure 4.** Optical spectroelectrochemistry of  $WO_3 \cdot H_2O$  (a, c) and  $WO_3$  (b, d) in 0.1 M TBAP in PC as a function of applied potential (V vs.  $Ag/Ag^+$ ). a, b) Optical transmittance as a function of applied potential for  $WO_3 \cdot H_2O$  and  $WO_3$ , respectively. c, d) Linear plots of optical transmittance at 550 nm (red, VIS region) and 1200 nm (blue, NIR region) as a function of applied potential.

To further understand the electrochemical processes responsible for the optical changes, we performed cyclic voltammetry of WO<sub>3</sub>·H<sub>2</sub>O and WO<sub>3</sub> film electrodes in 1 M LiClO<sub>4</sub> in PC (**Figure** 

3e, f, Figure S7). WO<sub>3</sub>·H<sub>2</sub>O exhibits mostly a potential-independent response: the low current between 3.4 and 3.5 V is associated with electric double layer formation on a lightly doped semiconducting material. Below 3.4 V and before the cathodic peak at 2.4 V, the current increases as electrons fill the conduction band (with associated ion adsorption or insertion) and eventually plateaus when the material becomes conductive.33 This response can also be described as the insertion of Li<sup>+</sup>/e<sup>-</sup> into WO<sub>3</sub>·H<sub>2</sub>O via a solid solution process. In our prior work on H<sup>+</sup> and Li<sup>+</sup> insertion in WO<sub>3</sub>·H<sub>2</sub>O, we hypothesized that this extended solid solution regime (as compared to WO<sub>3</sub>, vide infra) occurs because structural water molecules stabilize the structure during ion insertion. 14,26 At ~ 2.45 V, there is a reversible peak and the material continues to exhibit mostly a potential-independent response with excellent reversibility of the current at the turnover potential, indicative of good kinetics in the film. WO<sub>3</sub> exhibits a more potential-dependent response between 3.5 and 2.5 V: the cathodic current is small until the first reduction peak at ~2.65 V. The total charge passed in the potential region of 3.5 to 2.8 V is 0.91 mC/cm<sup>2</sup>, compared to 2.3 mC/cm<sup>2</sup> for WO<sub>3</sub>·H<sub>2</sub>O over the same potential range (**Figure S8**). This indicates that WO<sub>3</sub> doesn't have an extended solid solution insertion regime before the first structural transition from the monoclinic to tetragonal phase. Below 2.65 V, the response of WO<sub>3</sub> is potential-independent which indicates that at this point the film is conductive. WO<sub>3</sub>·H<sub>2</sub>O exhibits a coulombic efficiency of over 99% for scan rates from 1 – 200 mV s<sup>-1</sup>. In WO<sub>3</sub>, the coulombic efficiency remains above 85% across all scan rates (Figure S9b). Areal capacity (mC cm<sup>-2</sup>) was calculated using the cathodic CV cycle and shows comparable capacities between both films (Figure S9a). At slow scan rates (1 – 10 mV s<sup>-1</sup>), WO<sub>3</sub>·H<sub>2</sub>O and WO<sub>3</sub> exhibit areal capacities of ~9.3 and ~11 mC cm<sup>-2</sup>, respectively. WO<sub>3</sub> has a higher theoretical specific capacity than WO<sub>3</sub>·H<sub>2</sub>O because it doesn't contain structural water.<sup>26</sup> Capacity in both materials shows an inverse relationship to scan rate and declines to ~7.6 and ~7.2 mC cm<sup>-2</sup> at 200 mV s<sup>-2</sup> for WO<sub>3</sub>·H<sub>2</sub>O and WO<sub>3</sub>, respectively. The

better capacity retention of WO<sub>3</sub>·H<sub>2</sub>O indicates that, as in prior work, the presence of structural water leads to better insertion kinetics.

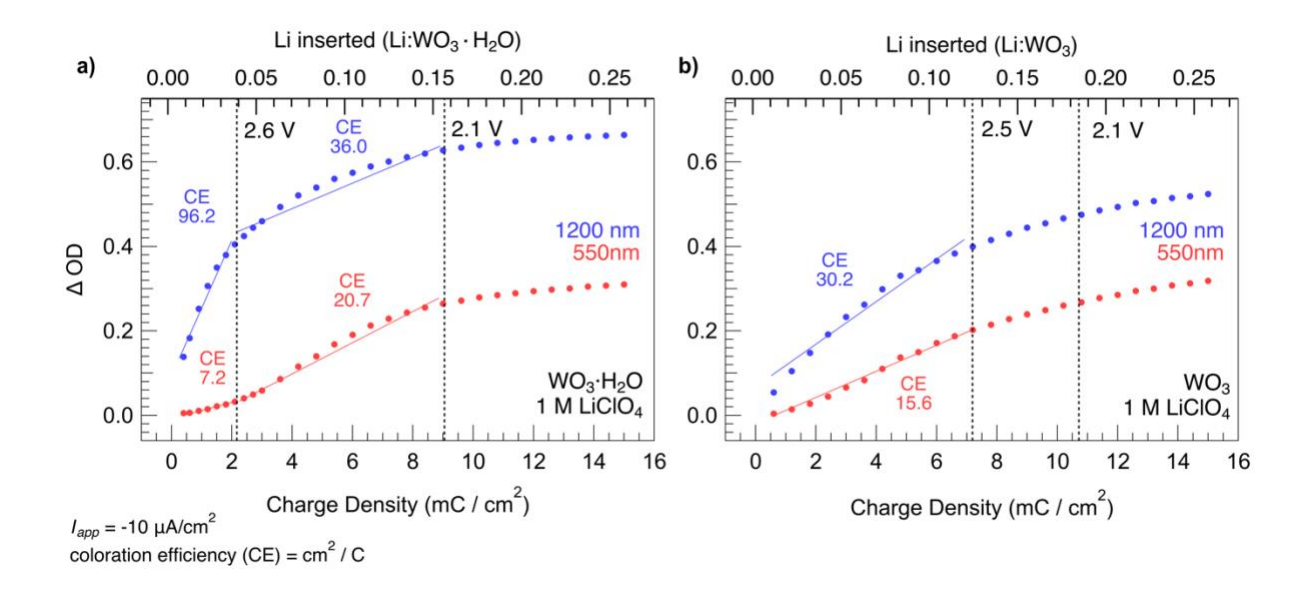


**Figure 5.** Coloration efficiency (CE) for  $WO_3 \cdot H_2O$  (a) and  $WO_3$  (b) measured at 550 nm (visible region) and 1200 nm (NIR region) to assess the change in optical density as a function of charge injected. Samples were electrochemically reduced in 1 M LiClO<sub>4</sub> in PC using an applied current of -10  $\mu$ A cm<sup>-2</sup>.

Next, we compared the CV features during the cathodic (coloration) sweep to changes in optical transmittance in LiClO<sub>4</sub> electrolyte. The potential-independent charge storage region of WO<sub>3</sub>·H<sub>2</sub>O between 3.5-2.6 V aligns with NIR light extinction, indicating that the solid-solution Li<sup>+</sup> insertion results in delocalized surface plasmon absorption and subsequent extinction of NIR light. The potential-dependent Li<sup>+</sup> insertion at ~2.6 V closely aligns with increasing visible light extinction (**Figure 3c and e**), indicating that higher amounts of Li<sup>+</sup> insertion lead to more localized charge storage and polaron absorption. The influence of structural water on the dual-mode electrochromic behavior of WO<sub>3</sub>·H<sub>2</sub>O in LiClO<sub>4</sub> in PC is further evidenced by the coloration

efficiency (CE), which is defined as the change in optical density ( $\Delta$ OD) as a function of injected charge. We assessed the  $\Delta$ OD as a function of injected charge at 550 nm (visible) and 1200 nm (NIR). At 550 nm, CE was only 7.2 cm<sup>2</sup> C<sup>-1</sup> at low Li<sup>+</sup> insertion (charge density < 2 mC cm<sup>-2</sup>), then increased to 20.7 cm<sup>2</sup> C<sup>-1</sup> at charge densities > 2 mC cm<sup>-2</sup> (**Figure 5a** red trace). At 1200 nm, CE was high (96.2 cm<sup>2</sup> C<sup>-1</sup>) at low charge density, then decreased to 36.0 cm<sup>2</sup> C<sup>-1</sup> at higher charge densities (> 2 mC cm<sup>-2</sup>, **Figure 5a** blue trace). Using electrochemical data, we determined the charge density of ~2 mC cm<sup>-2</sup> occurs at a potential of ~2.6 V vs Li/Li<sup>+</sup>, corresponding to the onset potential for the cathodic peak in WO<sub>3</sub>·H<sub>2</sub>O. This supports our conclusion that the Li<sup>+</sup> insertion induced phase transition in WO<sub>3</sub>·H<sub>2</sub>O marks an inflection point where Li<sup>+</sup> storage transitions from delocalized (capacitive-like) to localized (intercalation) charge storage, thereby shifting the electrochromic behavior from extinction primarily in the NIR to primarily in the visible region.

 $WO_3$  does not exhibit the same potential-independent  $Li^+$  insertion as  $WO_3 \cdot H_2O$  prior to its structural transition. In  $WO_3$ , the current response is negligible from 3.5 V until the cathodic peak at ~ 2.8 V. We hypothesize that the denser, 3D structure of  $WO_3$  undergoes an earlier structural change and/or lattice distortion to accommodate the insertion of  $Li^+/e^-$ , resulting in the single broadband spectral response.

We performed the same spectroelectrochemical analysis in 0.1 M TBACIO<sub>4</sub> in PC. The areal capacity in TBACIO<sub>4</sub> is considerably lower compared to LiClO<sub>4</sub>, which is expected given that charge storage is limited to surface reactions in TBACIO<sub>4</sub> electrolyte. At 1 mV s<sup>-1</sup>, the areal capacity for WO<sub>3</sub>·H<sub>2</sub>O and WO<sub>3</sub> are 4.6 and 3.6 mC cm<sup>-2</sup>, respectively (**Figure S10c**). The higher areal capacity of WO<sub>3</sub>·H<sub>2</sub>O than WO<sub>3</sub> in TBACIO<sub>4</sub> indicates a higher surface area, as expected from the SEM images. The CV shapes of WO<sub>3</sub>·H<sub>2</sub>O and WO<sub>3</sub> in TBACIO<sub>4</sub> are similar, and differ from those in LiClO<sub>4</sub>. The shapes are also unlike those expected for non-specific ion adsorption

(rectangular), and further investigation is needed to determine the exact mechanism associated with these electrochemical responses (**Figure S10a and b**). The CE in TBACIO<sub>4</sub> is significantly higher in the NIR region as compared to LiClO<sub>4</sub>, which suggests that although the overall charge density is low, all charge carriers are optically active (**Figure S11**). The CE of both films in TBACIO<sub>4</sub> are low in the visible region compared to the CE in the NIR region throughout charge injection because TBACIO<sub>4</sub> is limited to surface charging, and it cannot induce the polaronic absorption required for modulating changes in the visible region. Collectively, these results show that structural water plays an integral role in the dual-band electrochromic response of WO<sub>3</sub>·H<sub>2</sub>O. Extinction of NIR light occurs at low Li<sup>+</sup> insertion, because structural water leads to solid solution Li<sup>+</sup> insertion that results in surface plasmon resonance. At more reducing potentials, the electrochromic response is modulated in the visible region due to an electrochemically- induced structural transition that leads to localized charge storage and polaron absorption.

#### **Electronic structure calculations**

We performed DFT calculations to understand the changes in the optical properties due to Li\*/e-insertion into WO<sub>3</sub>·H<sub>2</sub>O and WO<sub>3</sub> thin films and their electronic structure origins. Using the transmittance spectra of WO<sub>3</sub> and WO<sub>3</sub>·H<sub>2</sub>O as a baseline, we computed the relative transmittance spectra after Li<sup>+</sup> insertion from the average of the contributions from the xx, yy and zz components (**Figure S12 and S13**). As shown in **Figure 6a** for WO<sub>3</sub>·H<sub>2</sub>O, the overall trend of the simulated relative transmittance agrees qualitatively with experiment, though with a significant underestimate. This is likely due to strong anisotropy in transmittance for Li<sub>0.12</sub>WO<sub>3</sub>·H<sub>2</sub>O, which shows much stronger absorbance in the zz direction than in the xx and yy directions (Figure S12). On the other hand, the simulated spectrum of Li<sup>+</sup>/e<sup>-</sup> insertion into WO<sub>3</sub> is in good agreement with the experiment (**Figure 6b**).

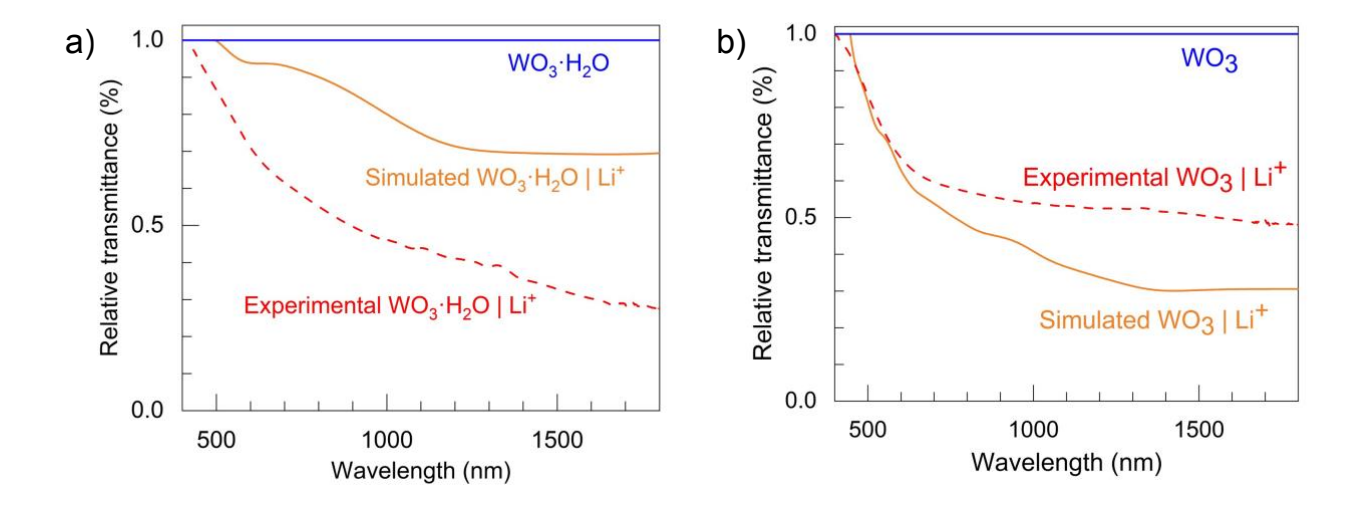


**Figure 6.** Comparison of DFT-simulated relative transmittance spectra with the experiment after Li<sup>+</sup> insertion for WO<sub>3</sub>·H<sub>2</sub>O (a) and WO<sub>3</sub> (b). The simulated compositions are Li<sub>0.12</sub>WO<sub>3</sub>·H<sub>2</sub>O and Li<sub>0.19</sub>WO<sub>3</sub>, compared to experimental Li<sub>0.11</sub>WO<sub>3</sub>·H<sub>2</sub>O and Li<sub>0.19</sub>WO<sub>3</sub>. The film thicknesses used in simulations are 250 nm and 80 nm, compared to experimental 243  $\pm$  34 nm and 78.5  $\pm$  0.7 nm, for WO<sub>3</sub>·H<sub>2</sub>O and WO<sub>3</sub>, respectively.

We further analyzed the density of states (DOS) for WO<sub>3</sub>·H<sub>2</sub>O and WO<sub>3</sub> before and after Li<sup>+</sup> insertion to determine the changes in electronic states after insertion. In the oxidized state, both materials exhibit semiconductor behavior with the valence band maximum (VBM) mainly consisting of O 2p states and the conduction band minimum (CBM) mainly consisting of W 5d states (Figure 7). Notably, in WO<sub>3</sub>·H<sub>2</sub>O, the VBM originates from O 2p states of WO<sub>3</sub> rather than H<sub>2</sub>O (Figure 7a). Upon Li<sup>+</sup> insertion, the Fermi level shifts upward, causing the bottom of the conduction bands to become occupied in both Li<sub>0.19</sub>WO<sub>3</sub> and Li<sub>0.12</sub>WO<sub>3</sub>·H<sub>2</sub>O (Figure 7b, d). A survey of the joint density of states (JDOS) provides information on the number of allowed optical transitions between the occupied conduction band electronic states and the unoccupied conduction band electronic states. The JDOS for both materials show that at ~400 – 1750 nm, Li<sub>0.19</sub>WO<sub>3</sub> and Li<sub>0.12</sub>WO<sub>3</sub>·H<sub>2</sub>O have a higher JDOS than oxidized WO<sub>3</sub> and WO<sub>3</sub>·H<sub>2</sub>O, implying that there is more photon absorption (Figure S14) and supports the conclusion that electrochromism

is attributed to intraband transitions from the occupied conduction band states to the higher lying unoccupied conduction bands.<sup>34–36</sup>

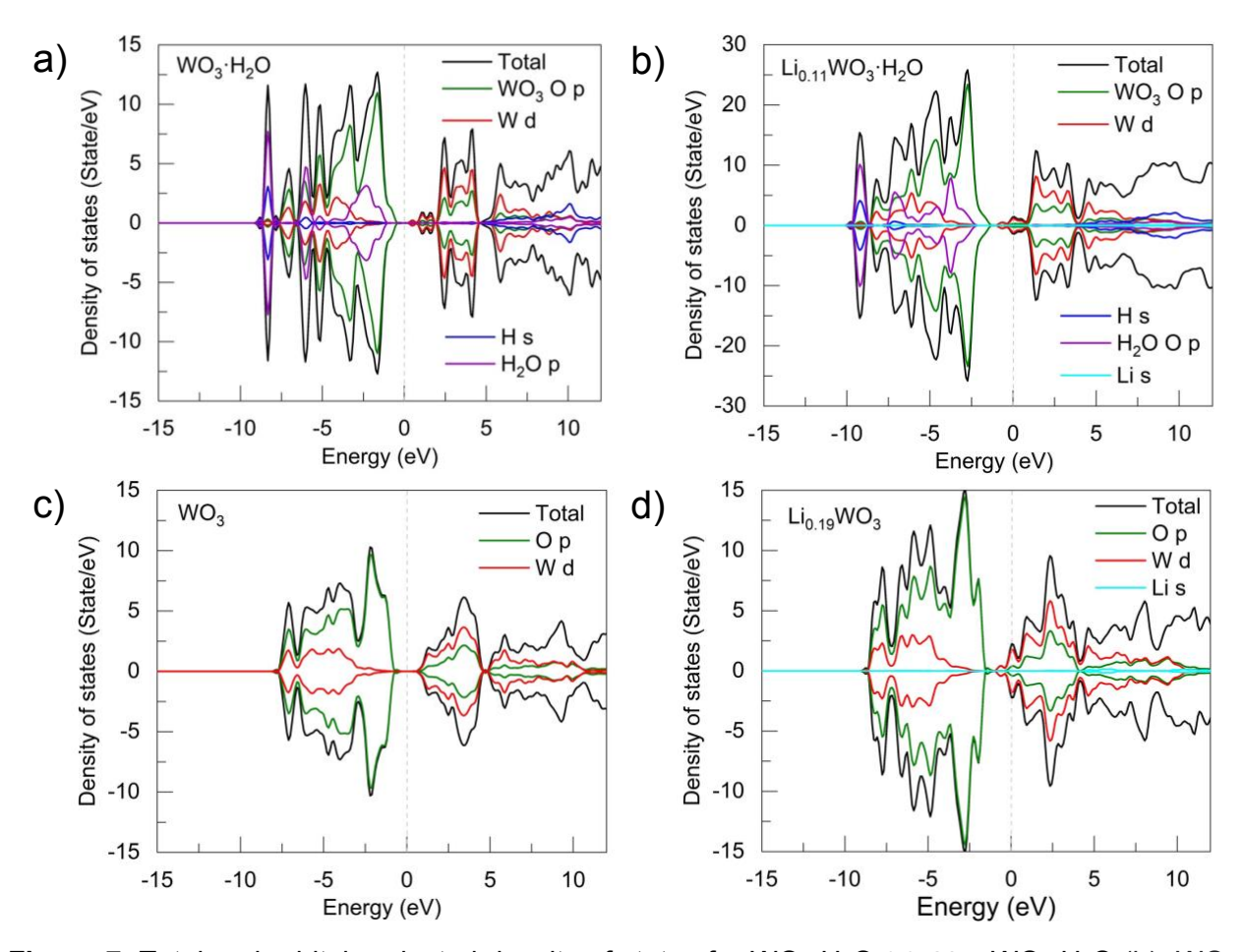


**Figure 7.** Total and orbital-projected density of states for  $WO_3 \cdot H_2O$  (a),  $Li_{0.11}WO_3 \cdot H_2O$  (b),  $WO_3$  (c), and  $Li_{0.19}WO_3$  (d). Energy is relative to the Fermi level (above dashed lines).

# **CONCLUSIONS**

In this study, we show that  $WO_3 \cdot H_2O$  exhibits dual-band electrochromic activity in the visible and NIR regime in a LiClO<sub>4</sub> /PC electrolyte due to its open crystal structure, in contrast to the broadband response of the denser  $WO_3$  (**Figure 8**). Dual-band behavior of  $WO_3 \cdot H_2O$  is attributed to a solid solution insertion regime that promotes delocalized charge storage of small cations (plasmon absorption/NIR) before a structural transition that leads to localized charge storage

(polaron absorption/VIS). We attribute the high potential solid solution regime to a more open structure (lower unit cell density) owing to the structural water in WO<sub>3</sub>·H<sub>2</sub>O. Anhydrous WO<sub>3</sub> is limited to single broadband behavior due to an early electrochemically-induced structural transition to accommodate the insertion of Li<sup>+</sup>/e<sup>-</sup> into the denser, 3D lattice. Determining structural features that promote dual-band electrochromism helps inform the design of single materials that can modulate the transmittance of visible and near-infrared (NIR) light independently, important for developing energy efficient smart windows.

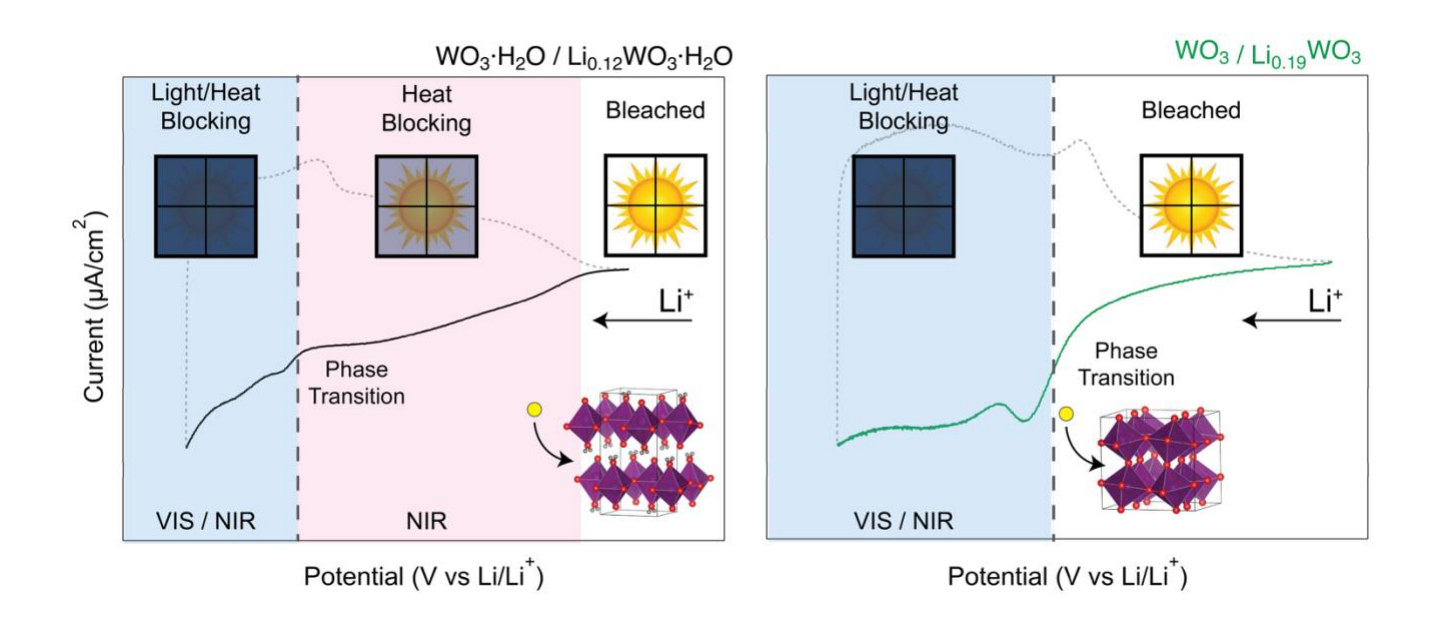


**Figure 8.** Summary schematic of the dual-band electrochromic response in  $WO_3 \cdot H_2O$  (left panel) compared to the broadband modulation in  $WO_3$  (right panel) as tungsten oxide is reduced in the presence of Li<sup>+</sup>. Dual-band modulation in  $WO_3 \cdot H_2O$  is facilitated by structural water, which creates an open crystal lattice for facile solid-solution reactions to occur before a phase transition that leads to modulation in the VIS.

## SUPPLEMENTARY INFORMATION

The data underlying this study (cyclic voltammetry, x-ray diffraction, Raman spectroscopy, scanning electron microscopy, spectroelectrochemistry, and DFT calculations) are openly available in Zenodo at https://doi.org/10.5281/zenodo.8087655.

The Supporting Information is available free of charge at:

Table S1: Suvey of Literature; Figure S1 – S3; Table S2: structural characterization; Table S3, DFT-optimized lattice parameters; Figure S4 -- S6, S11: Spectroelectrochemical characterization; Figure S7 – S10: electrochemical characterization; Figure S12 – S14: computational modeling

## **CONFLICT OF INTEREST**

The authors declare no known conflict of interest.

## **ACKNOWLEDGEMENTS**

The authors thank Michael A. Spencer for performing scanning electron microscopy. J.F., M.C, and V.A. acknowledge the support of the National Science Foundation under Grant No. 1653827. This work was performed in part at the Analytical Instrumentation Facility (AIF) at North Carolina State University, which is supported by the State of North Carolina and the National Science Foundation (award number ECCS-2025064). The AIF is a member of the North Carolina Research Triangle Nanotechnology Network (RTNN), a site in the National Nanotechnology Coordinated Infrastructure (NNCI). B. Z. Z. and D. J. M. acknowledge support from the Welch

Foundation (F-1848). DFT computation (M. L. and D. J.) was supported by the U.S. Department of Energy, Office of Science, Office of Basic Energy Sciences (award number DE-SC0023408).

#### **REFERENCES**

- (1) Yang, G.; Zhang, Y. M.; Cai, Y.; Yang, B.; Gu, C.; Zhang, S. X. A. Advances in Nanomaterials for Electrochromic Devices. *Chem. Soc. Rev.* **2020**, *49* (23), 8687–8720.
- (2) Llordés, A.; Garcia, G.; Gazquez, J.; Milliron, D. J. Tunable Near-Infrared and Visible-Light Transmittance in Nanocrystal-in-Glass Composites. *Nature* **2013**, *500* (7462), 323–326.
- (3) Tandon, B.; Lu, H. C.; Milliron, D. J. Dual-Band Electrochromism: Plasmonic and Polaronic Mechanisms. *J. Phys. Chem. C* **2022**, *126* (22), 9228–9238.
- (4) Judeinstein, P.; Livage, J. Study of the Electrochemical Mechanism in Tungsten Oxide Thin Films. *J. Chem. Phys.* **1993**, *90*, 1137–1147.
- (5) Kattouf, B.; Frey, G. L.; Siegmann, A.; Ein-Eli, Y. Enhanced Reversible Electrochromism via in Situ Phase Transformation in Tungstate Monohydrate. *Chem. Commun.* **2009**, No. 47, 7396–7398.
- (6) Heo, S.; Dahlman, C. J.; Staller, C. M.; Jiang, T.; Dolocan, A.; Korgel, B. A.; Milliron, D. J. Enhanced Coloration Efficiency of Electrochromic Tungsten Oxide Nanorods by Site Selective Occupation of Sodium Ions. *Nano Lett.* 2020, 20 (3), 2072–2079.
- (7) Zydlewski, B. Z.; Lu, H. C.; Celio, H.; Milliron, D. J. Site-Selective Ion Intercalation Controls Spectral Response in Electrochromic Hexagonal Tungsten Oxide Nanocrystals. *J. Phys. Chem. C* **2022**, *126* (34), 14537–14546.
- (8) Zhang, S.; Peng, Y.; Zhao, J.; Fan, Z.; Ding, B.; Lee, J. Y.; Zhang, X.; Xuan, Y. Amorphous and Porous Tungsten Oxide Films for Fast-Switching Dual-Band Electrochromic Smart Windows. *Adv. Opt. Mater.* **2022**, *2202115*, 1–8.
- (9) Lu, H. C.; Katyal, N.; Henkelman, G.; Milliron, D. J. Controlling the Shape Anisotropy of Monoclinic Nb<sub>12</sub>O<sub>29</sub> Nanocrystals Enables Tunable Electrochromic Spectral Range. *J. Am. Chem. Soc.* **2021**, *143* (38), 15745–15755.
- (10) Niklasson, G. A.; Granqvist, C. G. Electrochromics for Smart Windows: Thin Films of Tungsten Oxide and Nickel Oxide, and Devices Based on These. *J. Mater. Chem.* **2007**, 17 (2), 127–156.
- (11) Reichman, B.; Bard, A. J. The Electrochromic Process at WO₃ Electrodes Prepared by Vacuum Evaporation and Anodic Oxidation of W. *J. Electrochem. Soc.* **1979**, *126* (4), 583–591.
- (12) Kulesza, P. J.; Faulkner, L. R. Electrochemical Preparation of Electrodes Modified with Non-Stoichiometric Mixed-Valent Tungsten(VI, V) Oxides. *J. Electroanal. Chem.* **1988**, 248 (2), 305–320.
- (13) Wang, Z.; Gong, W.; Wang, X.; Chen, Z.; Chen, X.; Chen, J.; Sun, H.; Song, G.; Cong, S.; Geng, F.; Zhao, Z. Remarkable Near-Infrared Electrochromism in Tungsten Oxide Driven by Interlayer Water-Induced Battery-to-Pseudocapacitor Transition. ACS Appl. Mater. Interfaces 2020, 12 (30), 33917–33925.
- (14) Mitchell, J. B.; Geise, N. R.; Paterson, A. R.; Osti, N. C.; Sun, Y.; Fleischmann, S.; Zhang, R.; Madsen, L. A.; Toney, M. F.; Jiang, D. E.; Kolesnikov, A. I.; Mamontov, E.; Augustyn, V. Confined Interlayer Water Promotes Structural Stability for High-Rate

- Electrochemical Proton Intercalation in Tungsten Oxide Hydrates. *ACS Energy Lett.* **2019**, *4* (12), 2805–2812.
- (15) Mitchell, J. B.; Wang, R.; Ko, J. S.; Long, J. W.; Augustyn, V. Critical Role of Structural Water for Enhanced Li<sup>+</sup> Insertion Kinetics in Crystalline Tungsten Oxides . *J. Electrochem. Soc.* **2022**, *169* (3), 030534.
- (16) Shi, S.; Teng, F.; Hao, W.; Gu, W.; Yang, Z.; Zhao, F. Influence of Crystal Water on Crystal Structure, Electronic Structure, Band Structure, and Charge Separation of WO3·2H2O Nanosheets. *Inorg. Chem.* **2019**, *58* (14), 9161–9168.
- (17) Timofeeva, E. V.; Tsirlina, G. A.; Petrii, O. A. Formation of Rechargeable Films on Platinum in Sulfuric Acid Solutions of Isopolytungstates. *Russ. J. Electrochem.* **2003**, 39 (7), 716–726.
- (18) Pugolovkin, L. V.; Cherstiouk, O. V.; Plyasova, L. M.; Molina, I. Y.; Kardash, T. Y.; Stonkus, O. A.; Yatsenko, D. A.; Kaichev, V. V.; Tsirlina, G. A. Electrodeposited Non-Stoichiometric Tungstic Acid for Electrochromic Applications: Film Growth Modes, Crystal Structure, Redox Behavior and Stability. *Appl. Surf. Sci.* **2016**, *388*, 786–793.
- (19) Coelho, A. TOPAS-Academic, Powder Diffraction. 2007, pp 312–317.
- (20) Momma, K.; Izumi, F. VESTA 3 for Three-Dimensional Visualization of Crystal, Volumetric and Morphology Data. *J. Appl. Crystallogr.* **2011**, *44* (6), 1272–1276.
- (21) Kresse, G.; Furthmuller, J. Efficient Iterative Schemes for Ab Initio Total-Energy Calculations Using a Plane-Wave Basis Set. *Phys. Rev. B* **1996**, *54* (16), 11169–11186.
- (22) Perdew, J. P.; Burke, K.; Ernzerhof, M. Generalized Gradient Approximation Made Simple. *Phys. Rev. Lett.* **1996**, *77* (18), 3865–3868.
- (23) Heyd, J.; Scuseria, G. E.; Ernzerhof, M. Hybrid Functionals Based on a Screened Coulomb Potential. *J. Chem. Phys.* **2003**, *118* (18), 8207–8215.
- (24) Hong, W. Q. Extraction of Extinction Coefficient of Weak Absorbing Thin Films from Special Absorption. *J. Phys. D. Appl. Phys.* **1989**, *22* (9), 1384.
- (25) Wang, V.; Xu, N.; Liu, J. C.; Tang, G.; Geng, W. T. VASPKIT: A User-Friendly Interface Facilitating High-Throughput Computing and Analysis Using VASP Code. *Comput. Phys. Commun.* **2021**, *267*, 108033.
- (26) Mitchell, J. B.; Lo, W. C.; Genc, A.; Lebeau, J.; Augustyn, V. Transition from Battery to Pseudocapacitor Behavior via Structural Water in Tungsten Oxide. *Chem. Mater.* 2017, 29 (9), 3928–3937.
- (27) Balázsi, C.; Pfeifer, J. Structure and Morphology Changes Caused by Wash Treatment of Tungstic Acid Precipitates. *Solid State Ionics* **1999**, *124* (1), 73–81.
- (28) Wang, R.; Chung, C. C.; Liu, Y.; Jones, J. L.; Augustyn, V. Electrochemical Intercalation of Mg<sup>2+</sup> into Anhydrous and Hydrated Crystalline Tungsten Oxides. *Langmuir* **2017**, 33 (37), 9314–9323.
- (29) Spencer, M. A.; Fortunato, J.; Augustyn, V. Electrochemical Proton Insertion Modulates the Hydrogen Evolution Reaction on Tungsten Oxides. *J. Chem. Phys.* **2022**, *156* (6), 064704-1–9.
- (30) Daniel, M. F.; Desbat, B.; Lassegues, J. C.; Gerand, B.; Figlarz, M. Infrared and Raman

- Study of WO<sub>3</sub> Tungsten Trioxides and WO<sub>3</sub>\*xH<sub>2</sub>O Tungsten Trioxide Hydrates. *J. Solid State Chem.* **1987**, *67* (2), 235–247.
- (31) Granqvist, C. G. *Handbook of Inorganic Electrochromic Materials*; Granqvist, C. G., Ed.; Elsevier: Amsterdam, 1995.
- (32) Judeinstein, P.; Livage, J. Role of the Water Content on the Electrochromic Properties of WO<sub>3</sub>, nH<sub>2</sub>O Thin Films. *Mater. Sci. Eng. B* **1989**, 3 (1–2), 129–132.
- (33) Costentin, C.; Porter, T. R.; Savéant, J. M. Nature of Electronic Conduction in "Pseudocapacitive" Films: Transition from the Insulator State to Band-Conduction. *ACS Appl. Mater. Interfaces* **2019**, *11* (32), 28769–28773.
- (34) Faughnan, B.; Crandall, R.; Heyman, P. Electrochromism in WO<sub>3</sub> Amorphous Films. *RCA Rev.* **1975**, 36 (1), 177–197.
- (35) Kopp, L.; Harmon, B. N.; Liu, S. H. Band Structure of Cubic Na<sub>x</sub>WO<sub>3</sub>. *Solid State Commun.* **1977**, 22 (11), 677–679.
- (36) Hashimoto, S.; Matsuoka, H. Mechanism of Electrochromism for Amorphous WO<sub>3</sub> Thin Films. *J. Appl. Phys.* **1991**, 69 (2), 933–937.

# FOR TABLE OF CONTENTS USE ONLY

Title: Dual-Band Electrochromism in Hydrous Tungsten Oxide

**Authors:** Fortunato, Jenelle; Zydlewski, Benjamin; Lei, Ming; Holzapfel, Noah; Chagnot, Matthew; Mitchell, James; Lu, Hsin-Che; Jiang, De-en; Milliron, Delia; Augustyn, Veronica

**Description:** The TOC graphic shows the crystal structure of anhydrous tungsten oxide and monohydrate tungsten oxide and how the crystal structure influences their electrochromic properties for smart window applications. Monohydrate tungsten shows a dual band electrochromic response, whereas anhydrous tungsten oxide exhibits a single, broadband response.

